Journal of Non-Newtonian Fluid Mechanics 204 (2014) 7–21

Contents lists available at ScienceDirect

Journal of Non-Newtonian Fluid Mechanics

journal homepage: http://www.elsevier.com/locate/jnnfm

A new constitutive model for worm-like micellar systems – Numerical simulation of confined contraction–expansion flows

J.E. López-Aguilar [a,b], M.F. Webster [b,*], H.R. Tamaddon-Jahromi [b], O. Manero [c]

[a] Facultad de Química, Universidad Nacional Autónoma de México (UNAM), Mexico 04510, Mexico
[b] Institute of Non-Newtonian Fluid Mechanics, College of Engineering, Swansea University, Swansea SA2 8PP, United Kingdom
[c] Instituto de Investigaciones en Materiales, UNAM, Mexico 04510, Mexico

ARTICLE INFO

Article history:
Received 30 July 2013
Received in revised form 7 November 2013
Accepted 8 November 2013
Available online 24 November 2013

Keywords:
Rising excess pressure drop
Wormlike micelles
High-elasticity solutions
Bautista–Manero models
Hybrid finite element/volume method
Enhanced oil-recovery

ABSTRACT

This hybrid finite element/volume study is concerned with the modelling of worm-like micellar systems, employing a new micellar thixotropic constitutive model with viscoelasticity within network-structure construction–destruction kinetics. The work focuses on steady-state solutions for axisymmetric, rounded-corner, 4:1:4 contraction–expansion flows. This has importance in industrial and healthcare applications such as in enhanced oil-reservoir recovery. Material functions for the micellar models (*time-dependent, thixotropic*) have been fitted to match two different extensional configurations of the exponential Phan-Thien/Tanner (PTT) model (rubber *network-based, non-thixotropic*). This covers mild and strong-hardening response, and re solvent fraction, highly-polymeric ($\beta = 1/9$) and solvent-dominated ($\beta = 0.9$) fluids. Solution results are described through normalised Excess Pressure Drop (EPD), vortex intensity and stream function, stress (N_1 and N_2), and f-functional data. EPD predictions with the new micellar models prove to be consistent (at low rates, some rising) with Newtonian results, contrary to the base-reference modified Bautista–Manero (MBM) results. Markedly different vortex intensity trends are found in comparing micellar and EPTT solutions, which correspond with $N_2 - N_1$ and f data. In order to address the highly-elastic regime for thixotropic materials, a convoluted approach between EPPT and micellar models has been proposed. Here, numerically stable solutions are reported for impressively large *We* up to 300 and new vortex structures are revealed.

1. Introduction

This work is devoted to solve numerically the benchmark 4:1:4 rounded contraction/expansion flow of worm-like micellar systems using the Bautista–Manero constitutive approach [1–3]. Herein, a new approach is proposed that intimately introduces the viscoelasticity into the structure construction/destruction mechanism of worm-like micellar solutions. These non-Newtonian viscoelastic liquids present interactions of viscosity, elasticity, and breakdown and formation of internal structure. This spurns highly complex rheological phenomena, and manifests features associated with thixotropy, pseudo plasticity and shear-banding [1,5]. The versatility and complex rheological behaviour of viscoelastic wormlike micellar solutions render them an ideal candidate for varied applications. In viscoelastic surfactant form, they have been termed 'Smart Fluids', due to their ability to self-select their rheological properties to appropriately fit to change in alternative deformation environments. Processing and modern-day applications of such material systems range amongst additives in house-hold products (hard surface cleaners and drain-opener liquid plumber), paints, cosmetics, health care products (nutrient-carriers in shampoo and body wash), and under specific application fluid design such as with drag reducing agents in heating and cooling systems, and drilling fluids in enhanced oil-reservoir recovery (EOR) [6].

Significantly in modern EOR processes, which consist of hydraulic stimulation of oil wells to increase productivity, these fluid systems have become highly important given their adaptability in rheological characteristics [6]. Fracturing fluids are required in this operation, with the capability of transforming their rheological properties according to the prevailing flow conditions encountered. This involves transitions from low viscosity Newtonian fluids, when pumped into the oil-wells to fracture the rock-pores; passing through to gel-like form, with highly viscoelastic characteristics, capable of transporting proppants to keep fractures open and enhance rock-pores permeability in the oil-well; to finally, reverting into low viscosity fluids which degrade easily and unblock the fractures as the prerequisite pressure levels are realised. Wormlike micellar solution systems fulfil these requirements, being constituted of mixtures of surfactants – typically cetyltrimethylamonium bromide (CTAB) or cetylpyridinium chloride (CPyCl) [7] – and salts – sodium salicylate (NaSal) – in water.

* Corresponding author.
E-mail address: m.f.webster@swansea.ac.uk (M.F. Webster).

0377-0257/$ - see front matter © 2013 Elsevier B.V. All rights reserved.
http://dx.doi.org/10.1016/j.jnnfm.2013.11.001

These mixtures arrange themselves into physically bonded units and change their network-structure characteristics with temperature, surfactant and salt concentration [8]; but also with the forces and deformations they experience. The wormlike micelles are elongated surfactant groups that, under suitable conditions, can entangle and impart viscoelasticity to the fluid. Their behaviour is highly complex, although similar to that observed for polymer solutions and melts; hence their naming "living polymers" [8]. Unlike the covalently bonded polymer backbone, these micelles lie in thermodynamic equilibrium with the solvent and continuously break and reform under Brownian fluctuations. Therefore, additionally to reptation, wormlike micelles provide a mechanism for stress relief and entanglement elimination, creating and destroying temporary branch points, known as "ghost-like crossing" [8].

Furthermore, wormlike micelles are particularly viable for industrial application, since (a) fewer additives than for polymer-based fracturing fluids are required in their production, which render them a cheaper option [6]; (b) in EOR, chemical-breakers are unnecessary, since after contact with crude oil, wormlike micelles systems rearrange into small spherical micelles (c.a. 10–50 nm). These are simpler and smaller physical arrangements, which finally form a low viscosity microemulsion. Additionally, (c) wormlike micelles are more environmentally friendly and more easily biodegradable than polymer-based fracturing fluids [6].

Many approaches have been pursued to model wormlike micelles flow behaviour. Bautista et al. [1,2,4] proposed a rheological modelling approach for wormlike micelle solutions, the Bautista–Manero–Puig (BMP) model. This equation of state consists of the upper-convected Maxwell constitutive equation to describe stress evolution, coupled to a kinetic equation that takes into account structural changes induced by the flow, based on the rate of energy dissipation. This theory has demonstrated accuracy in the description of shear-banding [4,9,10], pulsating flows of wormlike micelle solutions [11], characterisation of associative polymers [12], and for evaluating the negative wake flow past a sphere [13] and drag correction [14]. Some years later, Boek et al. [3] corrected the BMP model, given its unbounded extensional viscosity in simple uniaxial extensional flow – thus producing the Modified Bautista–Manero (MBM) model. This has been utilised to model the transient flow of wormlike micellar solutions in planar 4:1 contraction flow setting [15], being a forerunner in wormlike micellar simulations for complex flows, along with others based on the principles of mesoscopic Brownian dynamics [16]. The VCM model, based on a discrete version of the 'living polymer theory' of Cates, has been tested in simple flows, where rheological homogeneity prevails [17,18], and under conditions of shear-banding [19]. Another approach, consists of using the Johnson–Segalman model, modified with a diffusion term for the extra/polymeric stress (so-called d-JS model [16,20–22]). This model has been tested against experimental data in simple shear flows and shear-banding conditions. The Giesekus model has also been used in the representation of wormlike micelles under simple shear scenarios, whilst using the non-linear anisotropy coupling parameter to introduce shear-banding conditions [23–28]. For this purpose, the appropriate Giesekus model parameters, for both banding and non-banding conditions, have been determined through Large Amplitude Oscillatory Shear (LAOS) [24] experiments in a coaxial-cylinder Couette geometry [23]. In addition, whilst using parallel plate geometries, and adjusting temperature, salt concentration and shear rate, shear-banding and non-banding conditions have been studied by Rheo-small-angle 1ight scattering (Rheo-SALS) [25], and flow-small angle neutron scattering (flow-SANS) [26]. In this respect, findings reveal shear-induced separation into an isotropic low-shear band and another flow-aligned nematic high-shear band.

The surfactant:salt concentration of these fluid-systems dictates their nature and rheological response, providing a classification into three (or more) basic types. As such, the so-called 'salt curve' provides the dependency of the zero-shear viscosity η_{p0} on the surfactant:salt concentration. Studies on the composition of wormlike micellar solutions and their rheological implications [29–31], provide evidence that these solutions (i) have η_{p0} close to the Newtonian solvent *at low salt concentration*; this range is characterised by *spherical micelles*. (ii) When the salt concentration is increased to *moderate/semi-dilute levels*, the solution demonstrates a dramatic increase in its zero-shear viscosity, reaching η_{p0} peaks as large as six times the solvent zero-shear viscosity [30,31]; this range manifests the formation-growth *of wormlike structures* and beginnings of their *entanglement*, causing shear-thinning and normal stresses in shear [31]. (iii) *Further increase of the salt concentration* generates *longer wormlike micelles*, which form an entangled network [31]. This is reflected in a steep decline in η_{p0} given by the proliferation of stress-relaxation points at the entanglement junctions [30]. The work presented in this manuscript is based around the Bautista–Manero approach [1–3,4], and aims to represent wormlike micellar systems in the second–third type-stage, with significant pseudoplastic and elastic characteristics. This theory originated to represent semi-dilute concentrations of micellar solutions in water, composed of erucyl bis-(hydroxyehtyl)methylammonium chloride (EHAC) as surfactant, and sodium salicylate (NaSal) as counterion [32]. In addition, such theory has proven effective more broadly to describe other micellar systems, such as cetylpyridinium chloride–sodium salicylate (CPCl) as surfactant, and brine as counterion; and cetyltrimethylammonium tosylate (CTAT), dodecyltrimethylammonium bromide (DTAB), Pluronics P103 as surfactants, with NaSal as counterion [33].

The contraction–expansion flow has become a standard benchmark problem in experimental and computational rheology [34]. Two of the most outstanding aspects to this configuration are the kinematics of flow, and the pressure drop measurement and its numerical estimation. The former is given by vortex activity in the re-entrant corner and the lip of the contraction. Here, diverse manifestations of the nature of the fluid can be outlined related in vortex size and evolution (extensional viscosity) and structure formation and numerical tractability (sharp/rounded corners) [15,35–37]. The pressure drop measurement, which reflects the energy expended in the flow, is often studied through an EPD measure [38,39], and offers a significant challenge to computational rheology [34,38].

Taking the experience gained in our prior work on modelling of wormlike micellar solutions [15], we subsequently deploy a new micellar approach, driven by phenomenological observation (EPD attainment) in the axisymmetric rounded-corner 4:1:4 contraction/expansion domain, for which there is a dearth of comparable work available – micellar fluid solutions in complex flows. This study also sheds light on some other key related topics – that is limiting *We* (We_{lim}) and vortex dynamics – all absent in simple viscometric flows [15,16]. We proceed to demonstrate that this new constitutive approach provides: (i) consistent EPD values at low *We* regimes – vital for oil-well rock-bed permeability estimation in EOR; (ii) larger We_{lim} in numerical solution reached through the explicit presence of the elasticity (*We*) in the structure equation; and (iii) attainment of rising EPD trends at high elasticity levels.

2. Governing equations, constitutive modelling and fluids considered

Under transient, incompressible and isothermal flow conditions, the relevant mass conservation and momentum equations for viscoelastic flow, may be expressed in non-dimensional terms (see definitions below; where here for conciseness the * notation on dimensionless variables is omitted) as:

$$\nabla \cdot \boldsymbol{u} = 0 \tag{1}$$

$$Re\frac{\partial \boldsymbol{u}}{\partial t} = \nabla \cdot \boldsymbol{T} - Re\boldsymbol{u} \cdot \nabla \boldsymbol{u} - \nabla p \tag{2}$$

where t represents time; the gradient and divergence operators apply over the spatial domain; field variables $\boldsymbol{u}$, p and $\boldsymbol{T}$ represent fluid velocity, hydrodynamic pressure and stress contributions, respectively; stress is split into solvent (viscous-inelastic) and polymeric contributions $\boldsymbol{T} = 2\eta_s\boldsymbol{D} + \boldsymbol{\tau}_p$; $\boldsymbol{D} = (\nabla\boldsymbol{u} + \nabla\boldsymbol{u}^{\dagger})/2$ is the rate of deformation tensor, where the superscript † denotes tensor transpose. The dimensionless variables utilised are defined as follows:

$$\boldsymbol{u}^* = \frac{\boldsymbol{u}}{U} \quad t^* = \frac{U}{L}t \quad \boldsymbol{\tau}_p^* = \frac{\boldsymbol{\tau}_p}{(\eta_{p0}+\eta_s)\frac{U}{L}} \quad p^* = \frac{p}{(\eta_{p0}+\eta_s)\frac{U}{L}} \quad \boldsymbol{D}^* = \frac{L}{U}\boldsymbol{D}$$

The non-dimensional group of the Reynolds number may be defined as $Re = \rho UL/(\eta_{p0} + \eta_s)$, with characteristic scales of U on fluid velocity (based on flow rate) and L on spatial dimension (based on minimum contraction dimension). Material density is ρ and reference viscosity is taken as the zero shear-rate viscosity, so that $\frac{\eta_{p0}}{\eta_{p0}+\eta_s} + \frac{\eta_s}{\eta_{p0}+\eta_s} = 1.0$. Here, η_{p0} is the zero rate polymeric viscosity and η_s is the solvent viscosity, from which the solvent fraction can be defined as $\beta = \eta_s/(\eta_{p0} + \eta_s)$.

A general statement of the differential constitutive model may be expressed in dimensionless form as [40]:

$$We\frac{\partial \boldsymbol{\tau}_p}{\partial t} = 2(1-\beta)\boldsymbol{D} - f\boldsymbol{\tau}_p - We(\boldsymbol{u}\cdot\nabla\boldsymbol{\tau}_p - \nabla\boldsymbol{u}^T\cdot\boldsymbol{\tau}_p - \boldsymbol{\tau}_p\cdot\nabla\boldsymbol{u}) \tag{3}$$

in which a second dimensionless group number is introduced governing elasticity, via a Weissenberg number ($We = \lambda_1 U/L$), which is a function of the characteristic material relaxation time, λ_1, and the characteristic velocity and length scales. By specifying the functional f, the network nature and theoretical properties of the fluid considered may be imposed into this general framework. Correspondingly, the exponential Phan-Thien Tanner (EPTT) model [41,42] has the following non-linear exponential form in the functional f:

$$f = exp\left(\frac{\varepsilon}{1-\beta}Wetr\boldsymbol{\tau}_p\right). \tag{4}$$

The constant, non-dimensional parameter ε largely dictates severity in strain-hardening, with smaller values limiting to zero, offering the greater extremes in extensional viscosity (larger Trouton ratios).

In the field of wormlike micellar systems, in the first instance, we adopt the modified Bautista–Manero (MBM) model [3]. This approach is based on the Bautista–Manero–Puig [1,2], in which a non-linear differential structure equation for the fluidity ($\phi_p = \eta_p^{-1}$), ultimately providing the polymeric viscosity η_p, dictates the construction/destruction dynamics of the structure of the fluid. Typically, this may begin from a fully structured state to be converted to a completely unstructured one, using the energy dissipated by the polymer under flow. This MBM model consists of a stress-split form, originally specified in dimensional form (see Eqs. (5)–(7)), in which the solvent contribution is of Newtonian-type and the polymeric contribution is given by the following expression:

$$\boldsymbol{\tau}_p + \frac{\eta_p}{G_0}\overset{\nabla}{\boldsymbol{\tau}}_p = 2\eta_p\boldsymbol{D}. \tag{5}$$

The structure equation is then:

$$\frac{\partial \eta_p^{-1}}{\partial t} = \frac{1}{\lambda_s}\left(\frac{1}{\eta_{p0}} - \frac{1}{\eta_p}\right) + \left(\frac{k}{\eta_\infty}\right)\boldsymbol{\tau}_p : \boldsymbol{D}. \tag{6}$$

Defining $f = (\eta_{p0}/\eta_p)$ using the zero-rate viscosity η_{p0} as a scaling factor, Eq. (6) can be recast into that to determine f, as follows:

$$\frac{\partial f}{\partial t} = \frac{1}{\lambda_s}(1-f) + \left(\frac{k}{\eta_\infty}\right)\eta_{p0}\boldsymbol{\tau}_p : \boldsymbol{D}. \tag{7}$$

Applying non-dimensionalisation (once more, omitting the * notation on dimensionless variables), as above, Eq. (5) takes the form of Eq. (3), and Eq. (7) now becomes:

$$\frac{\partial f}{\partial t} = \frac{1}{\omega}(1-f) + \xi_{\eta_{p0}}\boldsymbol{\tau}_p : \boldsymbol{D}. \tag{8}$$

The dimensionless parameters of this micellar model, which account for structural construction ($\omega = \lambda_s U/L$) and destruction ($\xi_{\eta_{p0}} = (k/\eta_\infty)\eta_{p0}(\eta_{p0}+\eta_s)U/L$), appear in the corresponding terms for these mechanisms.

In this study, we propose a *key* modification to Eq. (7) driven by phenomenological observation, which results in the *novel inclusion of viscoelasticity* within the destruction mechanics of the fluid structure, via $\eta_{p0} = G_0\lambda_1$. In the first instance, we develop the destruction term to accommodate only the energy in destroying the fluid structure from the polymeric dissipation (NM_τ_p model):

$$\frac{\partial f}{\partial t} = \frac{1}{\omega}(1-f) + \xi_{G_0}We\boldsymbol{\tau}_p : \boldsymbol{D} \tag{9}$$

where $\xi_{G_0} = (k/\eta_\infty)G_0(\eta_{p0}+\eta_s)$ is the new and replaced destruction dimensionless parameter.[1]

A second factor to consider is that there are contributions from both polymeric and solvent energy dissipation to the destruction of the fluid structure (NM_T model):

$$\frac{\partial f}{\partial t} = \frac{1}{\omega}(1-f) + \xi_{G_0}We\boldsymbol{T} : \boldsymbol{D}. \tag{10}$$

Finally, a hybrid modelling approach is pursued, by convoluting f-functionals of the EPTT and micellar models. Herein, a stronger, steady state f–We explicit relation is designed to attain high elasticity predictions for micellar fluids. For the steady-state case of the convolution of MBM and EPTT f-functionals (EPTT/MBM model) (see Table 1, for the other two variants):

$$f = (1 + \omega\xi_{\eta_{p0}}\boldsymbol{\tau}_p : \boldsymbol{D})exp\left(\frac{\varepsilon}{1-\beta}Wetr\boldsymbol{\tau}_p\right). \tag{11}$$

Material functions for the first four models in Table 1, along with the Oldroyd-B ($f = 1$) reference, are plotted in Fig. 1. Solvent fraction variants considered in this work are $\beta = \{1/9, 0.9\}$ for highly-polymeric and solvent-dominated fluids, respectively. The EPTT model parameters are chosen to take values at benchmark settings of $\varepsilon = \{0.25, 0.02\}$, characterising polymer melts and solutions [41], which are identified as applicable for moderate (MH, $\varepsilon = 0.25$) and strong hardening (SH, $\varepsilon = 0.02$) scenarios, respectively. The resulting micellar extensional viscosities are matched with those of corresponding EPTT forms at each $\{\varepsilon, \beta\}$ combination. The micellar combinations adopt the structure-construction parameter values of $\omega = 4.0$ for MH, and $\omega = 0.28$ for SH fluids. The structure-destruction parameter assumes different values for each micellar model depending on the solvent fraction, hardening characteristics and their matching to EPTT. The corresponding sets of parameters are listed in Table 1 for $\beta = \{1/9, 0.9\}$. Here, the distinction between parametric specification of NM_τ_p and NM_T models arises due to inclusion of the solvent contribution within the energy dissipation term, which introduces the further influence of the β-factor.

The material functions generated by the convoluted models are plotted in Fig. 2 for $\beta = 1/9$ and MH response (Table 1). Here, in Fig. 2a, the extensional and shear viscosity curves lie closer to those for EPTT. After the peak in extensional viscosity, at $We \sim 0.7$, the convoluted data provide larger extensional viscosity values than under MBM prediction, for which introduction of strain-softening is more abrupt. The EPTT/NM_T curve shows a steeper slope in the $20 < We < 400$ range; yet, there is little

[1] The corresponding theory may be developed for constructive contributions also, to be addressed subsequently.

Table 1
Parameter sets; highly-polymeric ($\beta = 1/9$), solvent-dominated fluids ($\beta = 0.9$).

Model – f-functional	$\beta = 1/9$		$\beta = 0.9$	
	MH	SH	MH	SH
EPTT				
$f = exp\left(\frac{\varepsilon}{1-\beta} We tr\boldsymbol{\tau}_p\right)$	$\varepsilon = 0.25$	$\varepsilon = 0.02$	$\varepsilon = 0.25$	$\varepsilon = 0.02$
MBM	$\omega = 4.0$	$\omega = 0.28$	$\omega = 4.0$	$\omega = 0.28$
$f = 1 + \omega\xi_{\eta p0}\boldsymbol{\tau}_p : \boldsymbol{D}$	$\xi_{\eta p0} = 0.1125$	$\xi_{\eta p0} = 0.1125$	$\xi_{\eta p0} = 1.0$	$\xi_{\eta p0} = 1.0$
*NM_*τ_p	$\omega = 4.0$	$\omega = 0.28$	$\omega = 4.0$	$\omega = 0.28$
$f = 1 + \omega\xi_{G_0} We\boldsymbol{\tau}_p : \boldsymbol{D}$	$\xi_{G0} = 0.1125$	$\xi_{G0} = 0.1125$	$\xi_{G0} = 1.0$	$\xi_{G0} = 1.0$
NM_T	$\omega = 4.0$	$\omega = 0.28$	$\omega = 4.0$	$\omega = 0.28$
$f = 1 + \omega\xi_{G_0} We\boldsymbol{T} : \boldsymbol{D}$	$\xi_{G0} = 0.1030$	$\xi_{G0} = 0.1100$	$\xi_{G0} = 0.1500$	$\xi_{G0} = 0.5800$
EPTT/MBM	$\varepsilon = 0.25$	–	$\varepsilon = 0.25$	–
$f = (1 + \omega\xi_{\eta p0}\boldsymbol{\tau}_p : \boldsymbol{D}) exp\left(\frac{\varepsilon}{1-\beta} We tr\boldsymbol{\tau}_p\right)$	$\omega = 4.0$ $\xi_{\eta p0} = 0.0010$		$\omega = 4.0$ $\xi_{\eta p0} = 0.010$	
*EPTT/NM_*τ_p	$\varepsilon = 0.25$	–	$\varepsilon = 0.25$	–
$f = (1 + \omega\xi_{G_0} We\boldsymbol{\tau}_p : \boldsymbol{D}) exp\left(\frac{\varepsilon}{1-\beta} We tr\boldsymbol{\tau}_p\right)$	$\omega = 4.0$ $\xi_{G0} = 0.0010$		$\omega = 4.0$ $\xi_{G0} = 0.010$	
EPTT/NM_T	$\varepsilon = 0.25$	–	$\varepsilon = 0.25$	–
$f = (1 + \omega\xi_{G_0} We\boldsymbol{T} : \boldsymbol{D}) exp\left(\frac{\varepsilon}{1-\beta} We tr\boldsymbol{\tau}_p\right)$	$\omega = 4.0$ $\xi_{G0} = 0.0010$		$\omega = 4.0$ $\xi_{G0} = 0.010$	

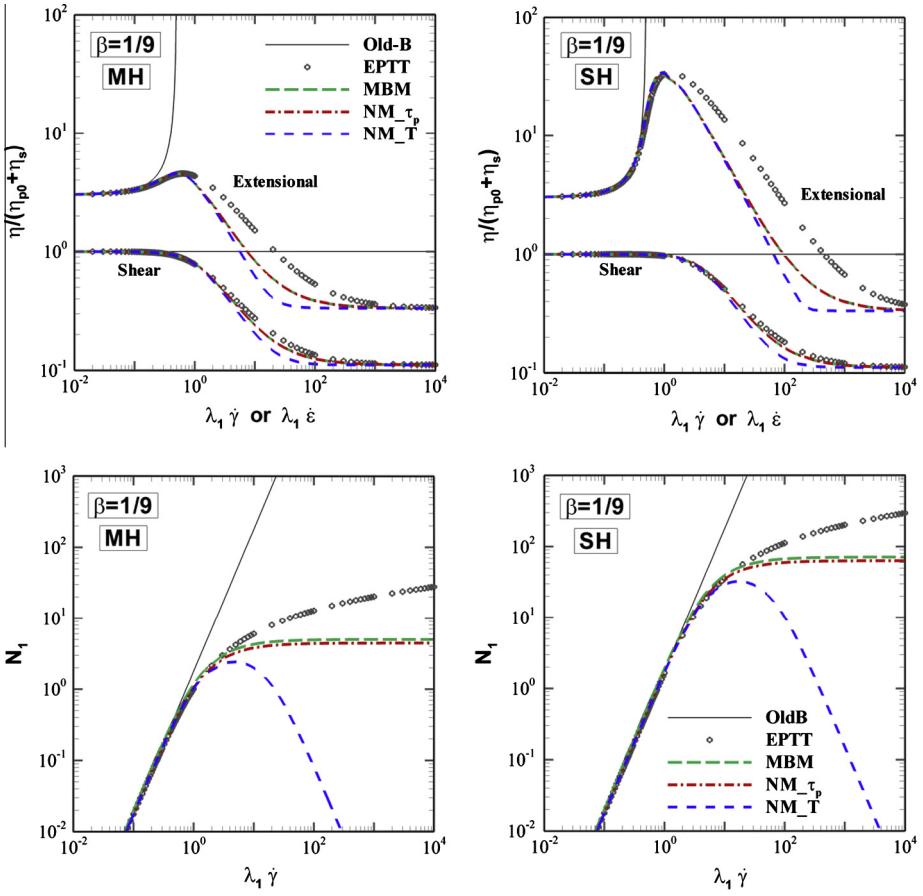

Fig. 1. Material functions versus *We*: top-shear and extensional viscosity, bottom-shear N_1; EPTT, MBM, NM_τ_p and NM_T models; *left*-MH (EPTT $\varepsilon = 0.25$; Micellar $\omega = 4.0$), *right*-SH (EPTT $\varepsilon = 0.02$; Micellar $\omega = 0.28$) response; highly-polymeric ($\beta = 1/9$) fluids.

difference observed outside this range with respect to the other convoluted cases. The MBM shear viscosity curve provides smaller values than the other curves for $We > 3$ onwards. On N_1 in shear (Fig. 2b), the convoluted data follow the nature of their non-convoluted pairs: the EPTT/MBM and EPTT/NM_τ_p curves inherit the MBM-plateau, with larger magnitude. The EPTT/NM_T curve peaks at $We \sim 40$ and declines thereafter with increasing *We*, as under NM_T prediction, which peaks at $We \sim 5$ (Fig. 1).

3. Problem specification and numerical scheme

3.1. The 4:1:4 rounded corner contraction/expansion flow

The schematic representation of the 4:1:4 axisymmetric, rounded-corner contraction/expansion flow problem with its corresponding zoomed mesh are shown in Fig. 3a and b, respectively. Mesh data are tabulated in Table 2. See Aguayo et al. [39] for

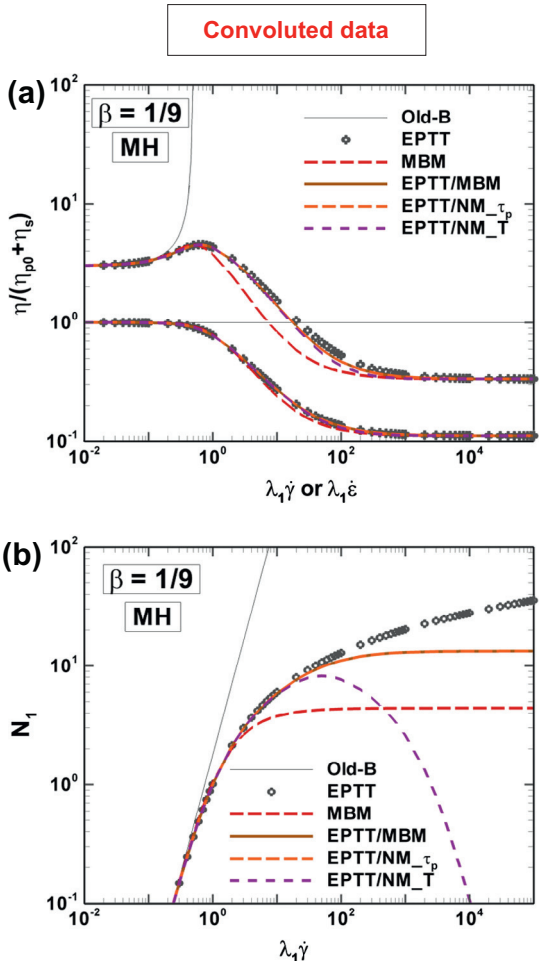

Fig. 2. (a) Shear and extensional viscosities, (b) shear N_1 versus We; MBM, EPTT and convoluted models; MH (EPTT $\varepsilon = 0.25$; Micellar $\omega = 4.0$) response, highly-polymeric ($\beta = 1/9$) fluids.

further detail on this problem, which provides a full mesh refinement analysis for some typical case studies.

3.2. Numerical scheme

The general framework of the time-marching hybrid *fe/fv* scheme employed here involves two distinct aspects. First, velocity and pressure are computed via a semi-implicit incremental pressure-correction (*ipc*) procedure with finite element spatial discretisation. Secondly, a finite volume based fluctuation distribution scheme is adopted for the computation of the hyperbolic extra-stress equations. The algorithm consists of a two-step Lax-Wendroff time-stepping procedure, extracted via a semi-implicit Taylor series expansion in time. The incremental pressure-correction signature is apparent through the three time-level pressure-reference. This ensures that temporal error bounds are uniformly met, to an order one higher than under direct *pc*-implementation, hence of $O(\Delta t^2)$ [43]. Here, first velocity and stress components are predicted to a half time-step (Stage 1a), and then, corrected over the full time-step (Stage 1b, Lax-Wendroff, split time-step, prediction–correction). To ensure the satisfaction of the incompressibility constraint, pressure at the forward time-step is derived from a Poisson equation for pressure-difference (Stage 2). The solenoidal end-of-time-step velocity field is constructed at a final stage (Stage 3). To attain second-order time accuracy, the free weighting parameter (θ), governing Stages 2 and 3 across the time-step, is

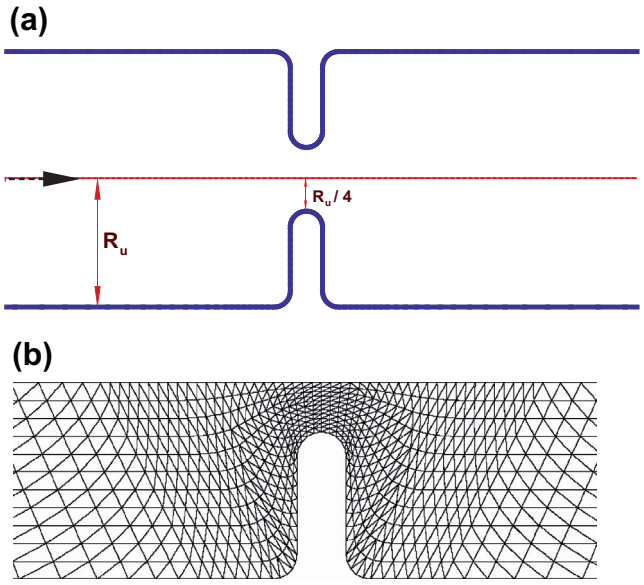

Fig. 3. (a) Schematic diagram, (b) zoomed mesh sections 4:1:4 contraction/expansion.

selected as the Crank-Nicolson option, ($\theta = 0.5$). Defining initial time-step (t^n) solution components $(u, p, \tau_p)^n$, the semi-discrete three-stage algorithmic structure per time-step may be expressed (omitting $*$ for dimensionless variables), as follows [44,45]:

Stage 1a:

$$\begin{aligned}
&\frac{2Re}{\Delta t}\left(\boldsymbol{u}^{n+\frac{1}{2}}-\boldsymbol{u}^{n}\right)=\left[\nabla\cdot\boldsymbol{\tau}_p-Re\boldsymbol{u}\cdot\nabla\boldsymbol{u}\right]^n-\nabla\left(p^n+\theta_1(p^n-p^{n-1})\right)+\nabla\cdot\left(2\beta\frac{\boldsymbol{D}^{n+\frac{1}{2}}+\boldsymbol{D}^n}{2}\right)+\boldsymbol{F}_G^n\\
&\frac{2We}{\Delta t}\left(\boldsymbol{\tau}_p^{n+1/2}-\boldsymbol{\tau}_p^n\right)=\left[2(1-\beta)\boldsymbol{D}-f\boldsymbol{\tau}_p-We\left(\boldsymbol{u}\cdot\nabla\boldsymbol{\tau}_p-\boldsymbol{\tau}_p\cdot\nabla\boldsymbol{u}-(\boldsymbol{\tau}_p\cdot\nabla\boldsymbol{u})^T\right)\right]^n\\
&\frac{2}{\Delta t}(f^{n+1/2}-f^n)=\left[\frac{1}{\omega}(1-f)+\zeta:\boldsymbol{D}\right]^n.
\end{aligned}\tag{12}$$

Stage 1b:

$$\begin{aligned}
&\frac{Re}{\Delta t}(\boldsymbol{u}^*-\boldsymbol{u}^n)=\left[\nabla\cdot\boldsymbol{\tau}_p-Re\boldsymbol{u}\cdot\nabla\boldsymbol{u}\right]^{n+\frac{1}{2}}-\nabla\left(p^n+\theta_1(p^n-p^{n-1})\right)+\nabla\cdot(2\beta\frac{\boldsymbol{D}^*+\boldsymbol{D}^n}{2})+\boldsymbol{F}_G^{n+\frac{1}{2}}\\
&\frac{We}{\Delta t}\left(\boldsymbol{\tau}_p^{n+1}-\boldsymbol{\tau}_p^n\right)=\left[2(1-\beta)\boldsymbol{D}-f\boldsymbol{\tau}_p-We\left(\boldsymbol{u}\cdot\nabla\boldsymbol{\tau}_p-\boldsymbol{\tau}_p\cdot\nabla\boldsymbol{u}-(\boldsymbol{\tau}_p\cdot\nabla\boldsymbol{u})^T\right)\right]^{n+\frac{1}{2}}\\
&\frac{1}{\Delta t}(f^{n+1}-f^n)=\left[\frac{1}{\omega}(1-f)+\zeta:\boldsymbol{D}\right]^{n+\frac{1}{2}}.
\end{aligned}\tag{13}$$

Stage 2:

$$\nabla^2(p^{n+1}-p^n)=\frac{Re}{\theta_2\Delta t}\nabla\cdot\boldsymbol{u}^*.\tag{14}$$

Stage 3:

$$\frac{2Re}{\Delta t}(\boldsymbol{u}^{n+1}-\boldsymbol{u}^*)=-\theta_2\nabla(p^{n+1}-p^n).\tag{15}$$

Here, ζ can take either $\xi_{\eta_0}\boldsymbol{\tau}_p$, $\xi_{G_0}We\boldsymbol{\tau}_p$ or $\xi_{G_0}We\boldsymbol{T}$ values, to specify MBM, NM_τ_p or NM_T models, respectively. With the EPTT model alone, the extra differential equation for f is replaced by the algebraic identity of EPTT-f (Eq. (4)); otherwise all model versions, including counterpart-convoluted, appeal to f (Eqs. (12), (13)).

4. Results and discussion

Discussion around the rising *We*-results solutions is based on findings under EPD, limiting *We* (We_{lim}), vortex dynamics, stress

Table 2
Mesh characteristics.

Mesh characteristics	Elements	Nodes	Degrees of freedom ($\boldsymbol{u}$, p, $\boldsymbol{\tau}_p$)	R_{min}
Coarse	1080	2289	14,339	0.0099
Medium	1672	3519	22,038	0.0074
Refined	2112	4439	27,798	0.0058

fields contours, and *f*-functional fields, considered against variation in rising *We*.

4.1. Excess pressure drop

4.1.1. Low solvent fraction conditions ($\beta = 1/9$)

The first point to highlight is the preservation of consistency in EPD in the Stokesian limit for the new versions of micellar models developed. In this limit of small deformation rates or vanishing elasticity, all fluids behave as the ideal universal fluid, for which non-linear characteristics vanish, and EPD (pressure drop measure relative to the equivalent Newtonian fluid) tends to the Stokes-Newtonian reference level of unity. Nevertheless, it is apparent from Fig. 4a that MBM EPD is inconsistent, providing $We \to 0$ limiting EPD values ~30% below the Stokes-Newtonian reference level. In contrast, EPTT models generate consistent EPD trends in the low elasticity asymptotic limit. With rising *We away from zero*, EPD-predictions generally tend to decrease and fall away from the Stokes-Newtonian reference EPD level (of unity); and this is upheld in MBM and EPTT solutions.

As described in Section 2, here new versions of micellar models are developed to address the MBM-shortcoming in EPD when $We \to 0$, which incorporate the viscoelasticity in the structure-destruction term, with explicit dependency on the *We*-factor [see Eq. (9) and Eq. (10), Fig. 4a]. Conspicuously then, and in contrast to the MBM-results, both micellar approaches (NM_τ_p and NM_T) do not exhibit underprediction in EPD in the low *We*-range. NM_τ_p solutions provide EPD values tightly matching in trend to EPTT predictions. Subsequently, upon rise in *We* there is: (i) a slight deviation to lower EPD from EPTT data in the $0 < We < 3$ range; (ii) NM_τ_p data attains critical solutions to $We_{lim} = 4.9$ (Table 3), where both NM_τ_p and EPTT curves intersect. In contrast when considering NM_T against EPTT solutions, some new EPD trends are gathered as *We* rises: (i) there is less degradation observed in EPD with NM_T than with EPTT, from the reference-line and in the low elasticity range ($0 < We < 3.5$); (ii) intersection between their respective EPD-curves occurs at a lower elasticity level ($We \sim 3.5$), taken relative to the NM_τ_p comparison. From $We \geqslant 3.5$ onwards, both NM_T and EPTT data-curves decline, but the loss of slope in EPD is more rapid with NM_T than EPTT as *We* rises; thus predicting ultimately larger EPD with NM_T for higher *We* up to $We_{lim} = 16$. These differences in EPD and We_{lim} attainments with new micellar versions (_τ_p and _T) can be explained by appealing to their respective material functions (Fig. 1), and analysing the competing influences of extensional viscosity (strain-hardening) and normal stress difference on EPD [46]. Whilst the NM_τ_p data-curve provides a plateau in N_1 for high *We* (Fig. 1), following the MBM results; the NM_T data-curve reveals a maximum in N_1 at moderate elasticity levels ($We \sim 5$), followed by a sharp decline over the extended range, $5 < We < 100$. This major disparity, firstly, generates lower stresses under NM_T compared with NM_τ_p solutions; consequently, yielding higher We_{lim} with NM_T than NM_τ_p. Secondly, as the competing roles between extensional viscosity (η_E) and N_1 in EPD predictions dictate [46] – rise in the former (strain-hardening) elevates EPD whilst it is weakening in N_1 (from quadratic form) that reinforces EPD. Therefore, the declining-N_1 of NM_T stimulates larger EPD than under

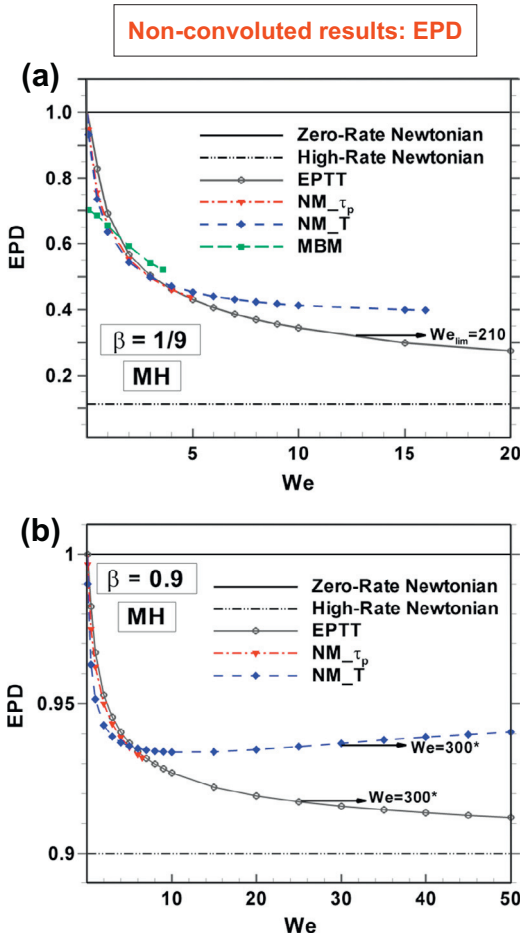

Fig. 4. EPD versus *We*; MBM, EPTT, NM_τ_p and NM_T models; (a) highly-polymeric ($\beta = 1/9$) and (b) solvent-dominated ($\beta = 0.9$) fluids; MH (EPTT $\varepsilon = 0.25$; Micellar $\omega = 4.0$) response.

Table 3
Limiting *We*; highly-polymeric ($\beta = 1/9$), solvent-dominated fluids ($\beta = 0.9$).

Model	$\beta = 1/9$		$\beta = 0.9$	
	MH	SH	MH	SH
EPTT	210.0	3.6	300.0[a]	4.6
MBM	3.6	1.8	4.1	2.2
NM_τ_p	4.9	2.1	7.6	2.4
NM_T	16	2.2	300[a]	30.0
EPTT/MBM	217	–	300[a]	–
EPTT/NM_τ_p	224	–	300[a]	–
EPTT/NM_T	300[a]	–	300[a]	–

[a] Stable solution.

EPTT-solutions, acknowledging that EPTT provides monotonically rising viscometric N_1 (itself with decay away from quadratic response). All comments apply equally under both strong and moderate-hardening settings, with exaggeration to higher η_E and N_1-maxima under the strong-setting.

In Fig. 5a, EPD predictions with convoluted models are reported, with restriction to MH-response and highly-polymeric ($\beta = 1/9$) fluids, and compared to those for base-EPTT and NM_T forms. Here, convoluted EPD data-curves principally inherit their parent-EPTT trends. Contrastingly, the NM_T solutions begin to show marginally larger EPD predictions, with respect to convoluted results, upon approaching the early $We_{lim} = 16$ of NM_T. Notably, at high deformation rates, EPD predictions for the convoluted models are

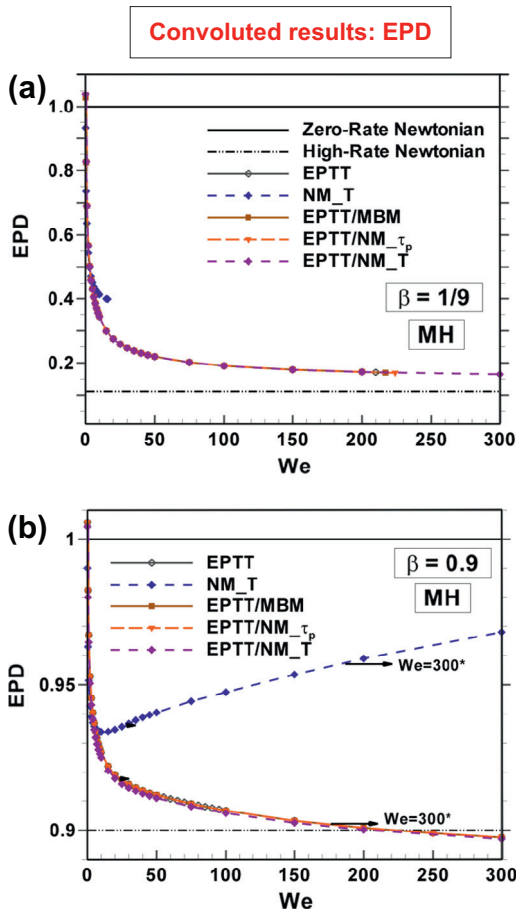

Fig. 5. EPD versus *We*; EPTT, NM_T and convoluted models; (a) highly-polymeric ($\beta = 1/9$) and (b) solvent-dominated ($\beta = 0.9$) fluids; MH (EPTT $\varepsilon = 0.25$; Micellar $\omega = 4.0$) response.

larger than the corresponding second-Newtonian EPD-plateau reference level indicated, and asymptote to a limiting plateau above that, accordingly.

4.1.2. High-solvent fraction conditions ($\beta = 0.9$)

In the high-solvent fraction scenario, with only mild strain-hardening properties and Newtonian-like response, NM_T solutions are observed to provide ultimately rising EPD trends with increasing elasticity (Figs. 4b and 5b). In contrast, NM_τ_p and EPTT solutions manifest only monotonic EPD-decline whilst traversing towards their We_{lim}. Similarly to the highly-polymeric scenario above, NM_τ_p solutions faithfully follow those of EPTT, locating their We_{lim} (=7.6) sooner than occurs with NM_T solutions, remaining numerically-stable at *We* = 300+ (Table 3). The reason for this discrepancy in We_{lim}, again as argued above with $\beta = 1/9$ fraction, lies in the base-N_1 material function response: recall, NM_T shows declining N_1 with rising *We*. This has the consequent effect of exhibiting a wider tractable window of numerical solution for NM_T, and favours the ultimate and opposite rising trend in EPD. This is the situation encountered beyond the local EPD-minima reached for NM_T at *We* = 8.

Under this high-solvent fraction, the *convoluted* data-curves again all follow those of parent-EPTT, and actually intersect with the second-Newtonian EPD-plateau reference line at high *We* levels, *We* ~ 220 (Fig. 5b). This latter observation contrasts with the distinctly different and remarkable NM_T model predictions (partially shown in Fig. 4b), which further pursue rising EPD trends with increasing elasticity levels (without encountering a limit).

4.2. Vortex dynamics

This section describes the various dynamic vortex structures developed in the flow, alongside their growth and decay patterns, through comparison across thixotropic and non-thixotropic models and their solutions at increasing levels of elasticity up to critical limits.

4.2.1. Vortex dynamics – low solvent fraction conditions ($\beta = 1/9$)

Here, a comparison on vortex intensity, size and streamlines patterns is performed as *We* is increased. To facilitate direct comparison, both upstream and downstream vortex intensities are plotted in Fig. 6 as a function of *We*.

4.2.1.1. Non-convoluted solutions, vortex intensity. Upstream vortex activity. MBM, NM_τ_p and NM_T data for the upstream vortex follow each other closely in a rising vortex intensity pattern with increasing *We*, up to their We_{lim} (Fig. 6a). NM_T solutions attain the largest We_{lim} (=16) amongst these micellar models, with indications of approach to an upper limiting plateau. Up to its first turning point at *We* = 2 (local maximum), EPTT results exhibit a similar trend to that of the thixotropic micellar solutions. Beyond which for *We* > 2, the EPTT data-curve indicates departure, initially through a decline to a second extremum at *We* = 100 (local minimum), prior to upturn and ultimate rise towards its final We_{lim} = 210 (Table 3) [36,37].

4.2.1.2. Non-convoluted solutions, downstream vortex activity. Downstream vortex activity mirrors, in reverse form, the changes in upstream vortex activity (Fig. 6b), somewhat acting as an energy balance and release mechanism. So here, thixotropic MBM, NM_τ_p and NM_T data-curves also follow each other closely in a declining trend up to *We* = 2. After this stage, NM_τ_p downstream vortex intensity declines suddenly and more rapidly than apparent with MBM or NM_T, noting that MBM is nearing its limit in this region at We_{lim} = 3.6, followed by NM_τ_p with We_{lim} = 4.9. The NM_T curve continues in its decline up to *We* = 7, where it observes a local-minimum. Beyond *We* > 7, NM_T downstream vortex intensity then rises up to its corresponding We_{lim} = 16. Conspicuously, the occurrence of this local minimum–extremum in the NM_T downstream vortex intensity response, roughly coincides in elasticity level (*We* = 7) with extrema observed in viscometric-N_1 for this model (*We* ~ 5) (Fig. 1). In contrast to micellar data, non-thixotropic EPTT results also exhibit a declining trend, but at slightly lower rate (hence, greater intensity), at relatively low elasticity levels (0.5 < *We* < 5). At *We* = 5, the EPTT data-curve also locates a minimum, beyond which for 7 < *We* < 15, the curve rises to a local-maximum at *We* = 15. After this second extremum, the trend is repeated of a subsequent decline, to find a third extremum (minimum) at 40 < *We* < 50. Finally and thereafter, the EPTT-curve rises up to its corresponding We_{lim} = 210.

Significant difference is apparent in We_{lim} between EPTT and MBM-solutions under MH: with $We_{lim} = O(10^2)$ for EPTT, and $We_{lim} = O(10)$ for micellar data (Table 3). One may argue that this is due to the explicit presence of λ_1 (or *We*, in dimensionless terms) in the *f*-functional under the EPTT construction. This discrepancy is starkly evidenced in MH instances, and through the comparison between the We_{lim} for MBM and the new micellar model data, where the presence of λ_1 increases We_{lim} by one unit for NM_τ_p, and increases eight times under NM_T (Table 3). This observation is not so evident under the SH scenario, yet still present, since We_{lim} is relatively small for the high extensional viscosity levels these fluid models can display.

4.2.1.3. Convoluted solutions, vortex intensity. The flow patterns displayed by the convoluted micellar solutions are markedly different to their non-convoluted counterparts; specifically, they inherit the

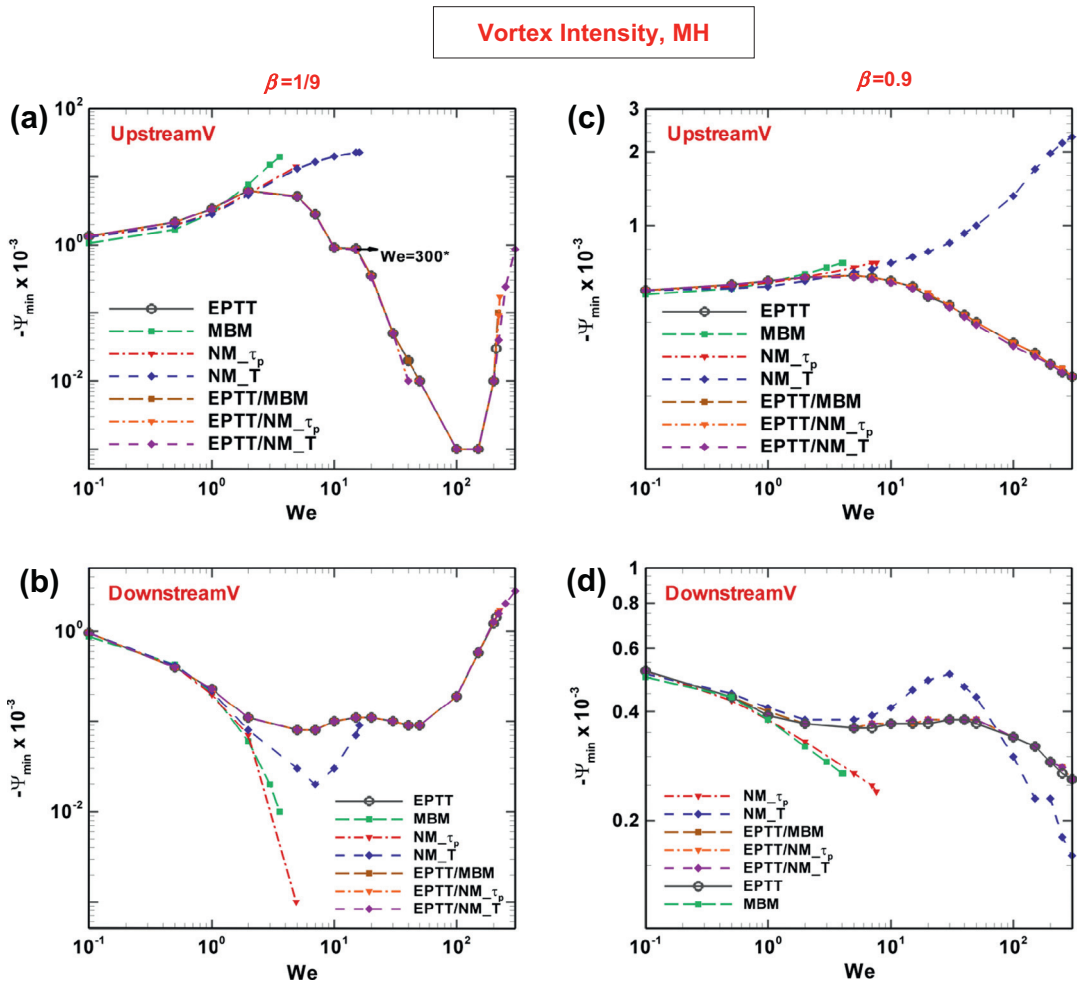

Fig. 6. Vortex intensity profiles versus *We*: top-upstream, bottom-downstream; EPTT, MBM, NM_τ_p, NM_T and convoluted models; MH (EPTT $\varepsilon = 0.25$; Micellar $\omega = 4.0$) response; highly-polymeric ($\beta = 1/9$), solvent-dominated ($\beta = 0.9$) fluids.

behavioural response of the parent-EPTT non-thixotropic predictions. On *upstream vortex* intensity (Fig. 6a), it is worth highlighting that (i) the convoluted data-curves follow closely over $0.1 < We < 300$ range; and (ii) after $We = 200$ and for stable EPTT/NM_T solutions, the upstream vortex reappears and monotonically grows in strength up to the corresponding We_{lim}, or $We = 300+$.

4.2.1.4. Convoluted solutions, downstream vortex intensity. In Fig. 6b, a more complex trend is extracted and relative to EPTT-solutions. Here, (i) the convoluted data-curves follow the trends for EPTT and lie between those the non-convoluted micellar data-curves; (ii) data-curves for convoluted solutions observe a local-minimum at $We = 7$, beyond which for $7 < We < 15$, they rise to a local-maximum at $We = 15$. After this second extrema, the trend is one of subsequent decline again to find a third extrema (minimum) at $40 < We < 50$. Finally, for $We > 50$, convoluted solutions show a monotonic rising trend up to their respective We_{lim}, with impressively high-*We* solutions generated for {EPTT/NM_τ_p, EPTT/MBM, EPTT/NM_T} with $We_{lim} = \{217, 224, 300+\}$ (Table 3). Comparatively, EPTT limitation is $We_{lim} = 210$, and with MBM is $We_{lim} = 3.6$, under the same solvent fraction ($\beta = 1/9$) and MH conditions. This trend also holds for the other convoluted results.

4.2.1.5. Streamline patterns, non-convoluted. The streamline patterns of Fig. 7, provide the counterpart field-structure representation to Fig. 6 above, in which the columns relate to variation across models, whilst the rows refer to levels of elasticity (terminating in We_{lim}). Results for *non-convoluted* forms are shown in Fig. 7. At low *We*-levels, $We \sim O(0.1)$, little difference is apparent in vortex size across models. Here, upstream and downstream vortex structures are symmetrical about the contraction. At $We = 1.0$, for which the elastic and dissipative forces are balanced, asymmetry is observed in all solutions, with slight differences in vortex sizes noted. These are clearly exposed in the vortex intensity data of Fig. 6 with increasing elasticity: whilst the upstream vortex displays vortex enhancement, the downstream vortex displays vortex reduction. Reaching the stage $We = 2$, where elastic effects are more dominant, this pattern of upstream growth/downstream shrinkage remains, and is reflected consistently in vortex size/shape across all solutions. MBM ($We_{lim} = 3.6$) results are the first to exhibit numerical breakdown. For higher elasticity levels, NM_τ_p (at $We = 4.9$) and NM_T (at $We = 5.0$) streamlines reflect upstream vortex growth, whilst EPTT results show shrinkage – notwithstanding the relatively even larger shear and extensional viscosities with EPTT (see N_1 and N_2 below for justification; nb. in contrast [36,37]). NM_τ_p results are the next in the sequence to show divergence ($We_{lim} = 4.9$), with an almost vanishing downstream vortex at this stage. Increasing elasticity to $We = 10$, the trends in vortex size evolution are well established. Consequently, NM_T ($We = 10$) results provide an even larger upstream vortex with $We < 10$, whilst comparably EPTT manifests vortex decay. The corresponding downstream vortex tends to disappear under

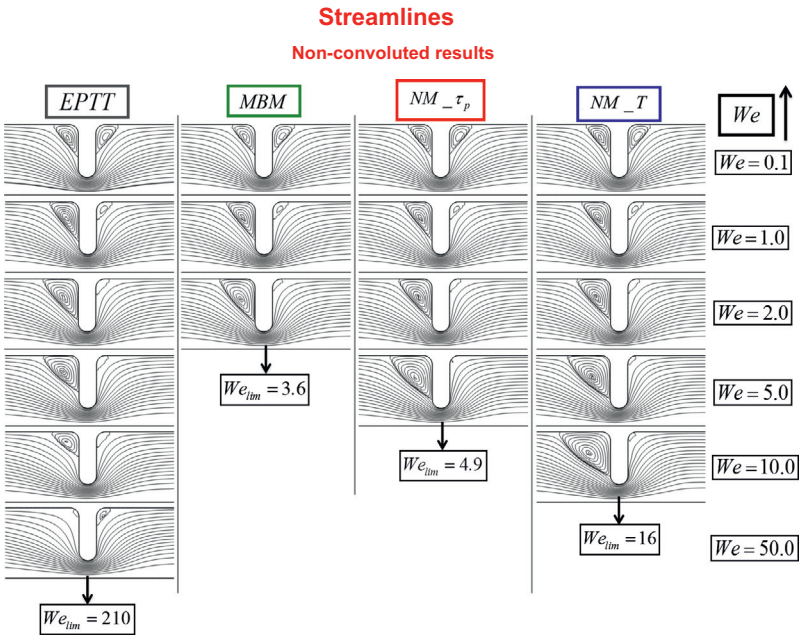

Fig. 7. Streamlines versus *We*; EPTT, MBM, NM_τ_p, NM_T models; MH (EPTT $\varepsilon = 0.25$; Micellar $\omega = 4.0$) response, highly-polymeric ($\beta = 1/9$) fluids.

NM_T, whilst that under EPTT prediction remains almost constant in size-shape as *We* rises. NM_T solutions locate their $We_{lim} = 16$. Finally, EPTT solutions retain tractability up to $We_{lim} = 210$; an impressively large level for stable numerical solutions.

4.2.1.6. Streamline patterns, convoluted. The streamlines in Fig. 8 for *convoluted* forms and data in Fig. 6 demonstrate that at $We = 200$, convoluted solution-fields exhibit the formation of a new upstream vortex (Fig. 8, inset). This grows and slightly shifts with *We*-rise, travelling towards the lip of the contraction wall. EPTT/NM_τ_p data at $We = 220$ reveals this new upstream vortex growth, and a further vortex structure appears from the top wall; both these new features then subsequently tend to join up with further *We* rise. In EPTT/NM_T results at $We = 300$, the upstream vortex appears completely formed, with comparable size to those at low elasticity levels ($1 < We < 5$), though now of one order of magnitude reduced in intensity. Meanwhile, as this complex upstream vortex activity is emerging, the downstream vortex shrinks over the $0.1 < We < 50$ range, and afterwards with further *We* rise, consistently and continually grows and builds in intensity.

4.2.2. Vortex dynamics – high solvent fraction conditions ($\beta = 0.9$); convoluted/non-convoluted results

Vortex intensity, $\beta = 0.9$ vortex intensity trends under solvent-dominated response ($\beta = 0.9$) (Fig. 6c and d) are similar, but with smaller values, to the corresponding highly-polymeric data ($\beta = 1/9$) (Fig. 6a and b). This applies in both *upstream and downstream* vortices.

The *upstream vortex intensity* results (Fig. 6c) exhibit smooth rise as *We* is increased at relatively low elasticity levels ($0.1 < We < 5$). Beyond $We > 5$, EPTT and convoluted solutions depart in trend and decline as *We* increases, with stable solutions at {$We = 300+$, $We_{lim} = 210$} for {$\beta = 0.9$, $\beta = 1/9$}. In this zone, the convoluted curves decline smoothly, whilst EPTT data-curve once more encounters a minimum, but now at $We = 200$. After this stage, EPTT suddenly rises up to $We = 250$, where it locates another extremum (maximum), and declines sharply-rapidly thereafter. Contrastingly, again, the non-convoluted thixotropic data-curves illustrate a rising pattern with increasing *We*, up to their We_{lim}.

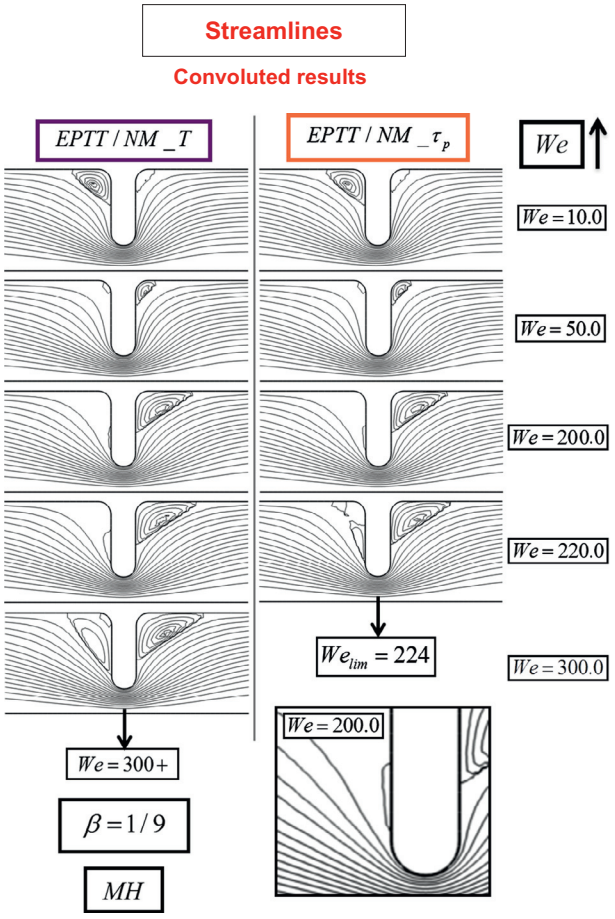

Fig. 8. Streamlines versus *We*; EPTT/NM_τ_p, EPTT/NM_T models; MH (EPTT $\varepsilon = 0.25$; Micellar $\omega = 4.0$) response, highly-polymeric ($\beta = 1/9$) fluids.

Differently to $\beta = 1/9$ results, the NM_T upstream data-curve now does not asymptote to a plateau. Here, at $\beta = 0.9$, {MBM, NM_τ_p, NM_T} attain $We_{lim} = \{4.1, 7.6, 300+\}$; in contrast at $\beta = 1/9$, {MBM,

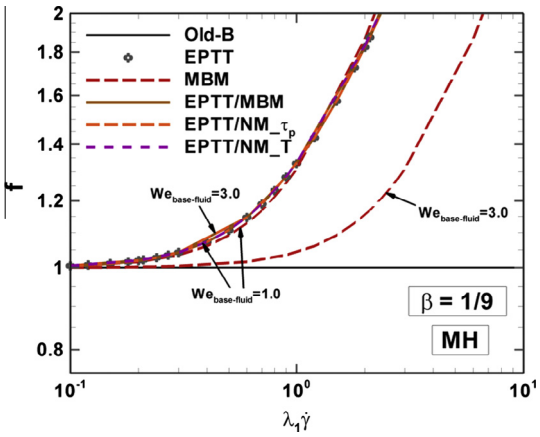

Fig. 9. *f*-Function profiles in simple shear versus *We*; MBM, EPTT and convoluted models; MH (EPTT $\varepsilon = 0.25$; Micellar $\omega = 4.0$) response, highly-polymeric ($\beta = 1/9$) fluids.

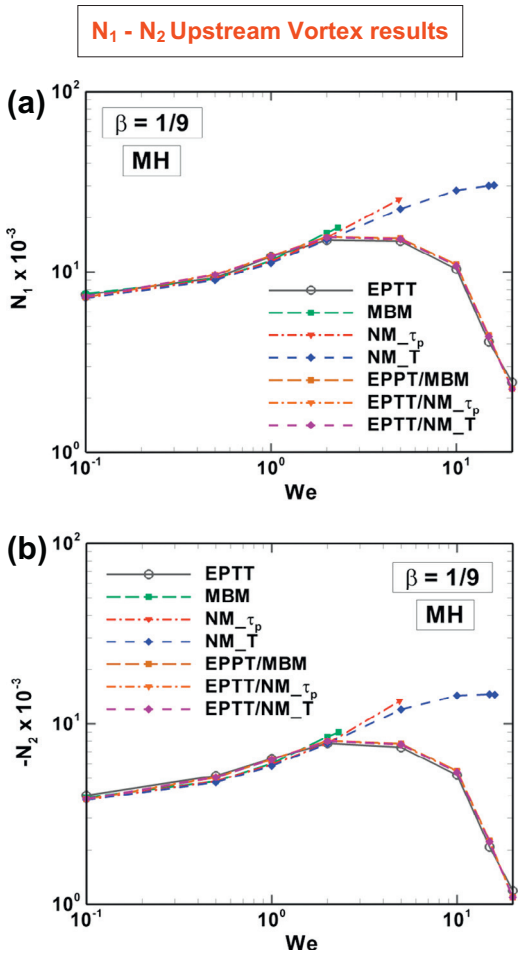

Fig. 10. (a) Maximum N_1 and (b) minimum N_2 versus *We*; EPTT, MBM, NM_τ_p, NM_T and the convoluted models; MH (EPTT $\varepsilon = 0.25$; Micellar $\omega = 4.0$) response, highly-polymeric ($\beta = 1/9$) fluids.

NM_τ_p, NM_T} encounter $We_{lim} = \{3.6, 4.9, 16\}$. Consistently, We_{lim} is notably extended under solvent-dominated predictions ($\beta = 0.9$), specifically in contrast to the highly-polymeric ($\beta = 1/9$) results above (Table 3 data). Recall, the non-linear polymeric part of the constitutive equation is present in smaller proportion, relative to the solvent contribution. Notably: (i) the NM_T extreme

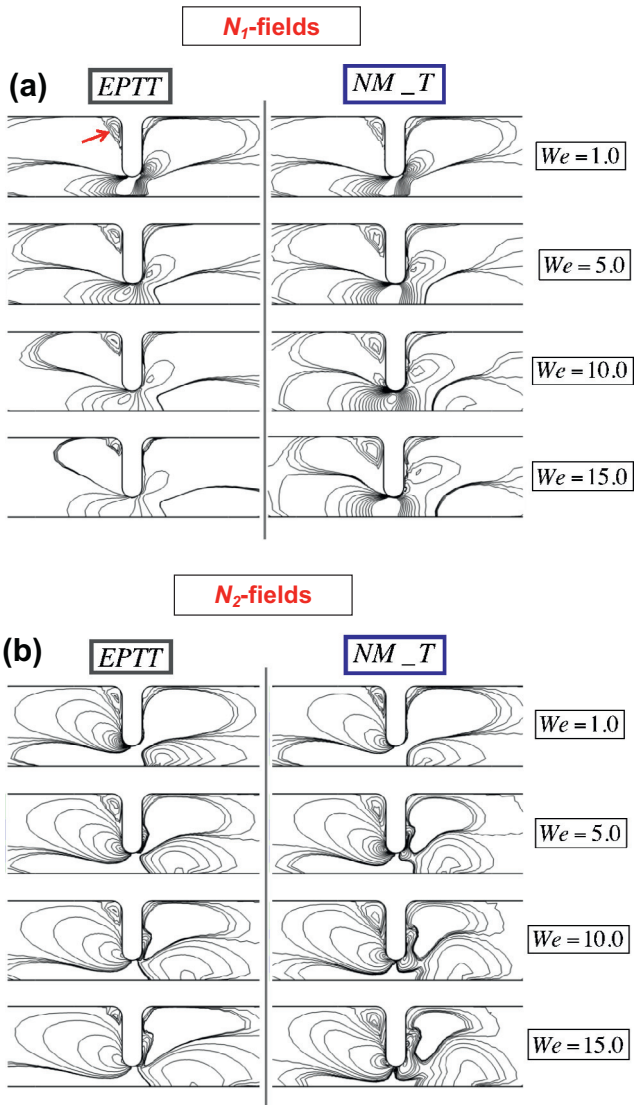

Fig. 11. (a) N_1 and (b) N_2 contour fields versus *We* comparison for EPTT and the NM_T models for MH (EPTT $\varepsilon = 0.25$; Micellar $\omega = 4.0$) response and highly-polymeric ($\beta = 1/9$) fluids.

case predicts that We_{lim} is some nineteen times larger under $\beta = 0.9$ than $\beta = 1/9$; (ii) such major departure in We_{lim} is also apparent between EPTT and most non-convoluted micellar results; and (iii) the common trends observed behind these We_{lim} findings repeat consistently under SH response (Table 3).

On *downstream vortex intensity* Fig. 6d, a declining trend is observed at low elasticity levels ($0.1 < We < 2$). Beyond $We > 2$, the following departure is observed: EPTT and convoluted results exhibit a local minimum at $We = 5$, and rise to locate a plateau in $20 < We < 50$. Beyond $We > 50$, an ultimate decline is apparent with the convoluted results, whereas EPTT evolves as with the upstream vortex data above. Conspicuously, the thixotropic non-convoluted results generate some alternative trends: {MBM, NM_τ_p}-data-curves decline as elasticity is increased up to their $We_{lim} = \{4.1, 7.6\}$. In contrast, the NM_T downstream vortex intensity pattern is more complex; resembling the EPTT and convoluted solutions. The NM_T data-curve plateaus across $2 < We < 5$ range; thereafter, this curve rises with increasing elasticity up to a peak of $We = 30$. Subsequently after this local peak, for $We > 30$, NM_T downstream vortex intensity ultimately declines, with stable solutions observed as far out as $We = 300+$ and above.

Table 4
Maximum and minimum *f*-function values versus *We*; MH (EPTT $\varepsilon = 0.25$; Micellar $\omega = 4.0$) response, highly-polymeric fluids ($\beta = 1/9$).

We		*f*						
		EPTT/NM_T	EPTT/NM_τ_p	EPTT/MBM	EPTT	MBM	NM_τ_p	NM_T
0.1	Max.	1.15	1.15	1.25	1.14	6.35	2.06	2.17
	Min.	0.98	0.98	0.99	1.00	0.99	1.00	1.00
0.5	Max.	2.50	2.49	2.53	2.46	5.82	4.11	5.00
	Min.	0.94	0.94	0.95	0.97	0.81	0.87	0.91
1.0	Max.	4.12	4.10	4.11	4.09	5.62	5.62	7.25
	Min.	0.91	0.91	0.91	0.96	0.60	0.59	0.69
2.0	Max.	6.86	6.80	6.76	6.81	5.62	7.40	9.77
	Min.	0.96	0.96	0.96	1.00	0.11	−0.34	0.05
5.0	Max.	13.55	13.43	13.39	13.24	D[b]	11.04[c]	13.74
	Min.	0.94	0.94	0.94	0.99		−4.92	−2.76
10.0	Max.	23.37	23.14	23.07	22.86		D	17.73
	Min.	0.92	0.92	0.92	0.95			−8.05
15.0	Max.	32.81	32.47	32.39	32.08			19.76
	Min.	0.95	0.95	0.95	0.94			−13.66
20.0	Max.	41.93	41.48	41.39	41.01			D
	Min.	0.96	0.96	0.96	0.94			
50.0	Max.	97.29	98.25	98.46	96.84			
	Min.	0.93	0.93	0.93	0.91			
100.0	Max.	192.22	196.08	196.53	179.78			
	Min.	0.86	0.86	0.86	0.86			
200.0	Max.	380.06	393.88	394.91	360.40			
	Min.	0.78	0.17	0.07	0.08			
220.0	Max.	417.08	433.75	D	D			
	Min.	0.76	0.005					
300.0	Max.	564.65	D[a]					
	Min.	0.09						

[a] Diverged.
[b] Diverged at $We_{lim} = 3.6$.
[c] Diverged at $We_{lim} = 4.9$.

4.3. *f*-Functional and stress fields (N_1)

4.3.1. Low solvent fraction conditions ($\beta = 1/9$)

In this section, results for *f*-functional and normal stress are considered. Firstly, correspondence between vortex activity (Section 4.2) and normal stresses data (i.e. N_2) is outlined. Secondly, *f*-functional and N_1 results are described, in which close correlation is revealed through theoretical and numerical data. Markedly, an inverse relation between N_1 and *f* predictions is observed with the numerical solutions for contraction–expansion flow, similar to that obtained in simple viscometric shear. Fig. 9 provides *shear viscometric f-functional data*, where all curves rise from the Oldroyd-B reference data as *We* is elevated. Consistently with their exponential nature, the response for EPTT and convoluted curves follow each other closely. Differently, (i) MBM-data yield smaller *f*-values in the $0.1 < \dot{\gamma} < 1.5$ range. For larger rates beyond $\dot{\gamma} > 1.5$, MBM form provides larger *f*-values than arise for EPTT and its convoluted analogues. (ii) As *We* rises, only MBM response shows decline in the size of *f*-values at fixed shear-rate.

4.3.2. N_2, N_1-vortex activity and relationship

Fig. 10 shows maximum N_1 and minimum N_2 in the *upstream vortex zone* across models as *We* is increased. Here, it is worth highlighting the correlation between N_2-minima and N_1-maxima observed in the upstream vortex region, alongside the location, size and intensity of the upstream vortices themselves. This provides concrete evidence as to the influence of elasticity in the flow kinematics. Solutions trends in N_1-maxima (Fig. 10a) and N_2-minima (Fig. 10b) correspond to those in Fig. 6a for maximum intensity in the upstream vortex. As above for vortex intensity, MBM, NM_τ_p and NM_T curves on N_1 and N_2 extrema in the upstream vortex, closely follow one another in a rising pattern with increasing *We* up to their We_{lim}. EPTT and convoluted results exhibit similar rising and further declining trends as *We* is elevated. Furthermore, N_2 results for convoluted versions (Fig. 10b) evidence larger values over $0.1 < We < 2$, and smaller values over $2 < We < 15$, in comparison to EPTT N_2-data. Beyond $We > 15$, a sudden and steeper slope is noted in the convoluted solutions. The vortex-like structures in N_1 and N_2-fields, are absent for $We > 20$ in the upstream zone, and disappear at low elastic levels in the downstream region. Hence, direct comparison with vortex patterns loses tractability beyond $We > 20$. Fig. 11 contains the counterpart field-structure representation of Fig. 10, with the key results for EPTT and NM_T solutions. Particularly, N_2 plots render the most illustrative information [47], providing a signature for vortex development in the corner-region (Fig. 11b), whilst N_1 plots (Fig. 11a) only show its periphery through location and relative size.

4.3.3. *f*-Functional expression, size of N_1 and impact on We_{lim}

As specified in Section 2, Eq. (3) provides a general form for the equation of state for stress, where the only essential difference is given by the *f*-functional. This functional takes into account departure from Oldroyd-B-like behaviour. As argued above, the explicit presence of λ_1 (or *We*, in dimensionless terms) in *f* is most important for these new micellar models (NM_τ_p and NM_T), since it provides consistent EPD values at low *We* and produces relatively large We_{lim}. Hence, it is pertinent to discuss the nature and role played by this explicit *f*–*We* functionality on solutions. As listed in Table 1, the EPPT model contains an explicit, *exponential f–We* relation in its constitutive equation (with $We_{lim} = 210$ under MH conditions, see Table 3). In comparison, an explicit, *linear f–We*

Table 5
Maximum and minimum N_1 dimensionless values versus *We*; MH (EPTT $\varepsilon = 0.25$; Micellar $\omega = 4.0$) response, highly-polymeric fluids ($\beta = 1/9$).

We		N_1						
		EPTT/NM_T	EPTT/NM_τ_p	EPTT/MBM	EPTT	MBM	NM_τ_p	NM_T
0.1	Max.	8.24	8.25	7.89	8.30	2.41	5.48	5.20
	Min.	−5.08	−5.08	−4.98	−5.09	−2.18	−4.18	−4.05
0.5	Max.	7.84	7.87	7.79	7.98	3.09	4.83	3.59
	Min.	−3.08	−3.08	−3.07	−3.09	−2.15	−2.64	−2.50
1.0	Max.	5.71	5.75	5.76	5.84	4.46	4.46	2.95
	Min.	−2.22	−2.22	−2.22	−2.23	−2.19	−2.20	−2.04
2.0	Max.	3.70	3.75	3.78	3.80	7.44	4.17	2.72
	Min.	−1.46	−1.46	−1.46	−1.46	−2.98	−1.77	−1.61
5.0	Max.	1.93	1.98	2.00	2.00	D[b]	4.11[c]	2.94
	Min.	−0.93	−0.93	−0.94	−0.94		−3.53	−1.72
10.0	Max.	1.15	1.18	1.20	1.20		D	3.01
	Min.	−0.66	−0.66	−0.67	−0.67			−2.26
15.0	Max.	0.83	0.87	0.88	0.88			3.03
	Min.	−0.49	−0.49	−0.50	−0.49			−2.02
20.0	Max.	0.67	0.70	0.70	0.70			D
	Min.	−0.40	−0.40	−0.40	−0.40			
50.0	Max.	0.33	0.34	0.34	0.34			
	Min.	−0.19	−0.20	−0.20	−0.20			
100.0	Max.	0.19	0.19	0.19	0.19			
	Min.	−0.11	−0.11	−0.11	−0.11			
200.0	Max.	0.11	0.11	0.11	0.11			
	Min.	−0.06	−0.06	−0.06	−0.06			
220.0	Max.	0.10	0.10	D	D			
	Min.	−0.06	−0.05					
300.0	Max.	0.07	D[a]					
	Min.	−0.04						

[a] Diverged.
[b] Diverged at $We_{lim} = 3.6$.
[c] Diverged at $We_{lim} = 4.9$.

functionality appears in the new micellar forms (NM_T with $We_{lim} = 16$, and NM_τ_p with $We_{lim} = 4.9$). The MBM model, which attains $We_{lim} = 3.6$, does not possess an explicit relationship between *f* and *We*. These observations suggest a possible correlation between *f* and We_{lim}: the stronger the *f*–*We* functional relationship (expressed in powers or rate-rise), the larger the We_{lim}. *Size of f-functional and N_1 forms across these micellar models* are provided in Table 4 and 5. NM_τ_p solutions (with $We_{lim} = 4.9$) generate larger N_1 (smaller *f*−) values than under NM_T (with $We_{lim} = 16.0$) at comparable elasticity levels. Furthermore, MBM solutions yields larger N_1 (smaller *f*−) values (with $We_{lim} = 3.6$) than under NM_τ_p prediction (with $We_{lim} = 4.9$) for $1 < We < 2$.

4.3.4. N_1 and f-functional fields, non-convoluted

Fig. 12a provides a complete record for the (N_1 *fields non-convoluted*) predictions. First, *EPTT-N_1 results* exhibit fields with vanishing negative zones and declining maximum values as *We* rises. This is consistent with (i) the inverse, quadratic relation between the *f*-functional and N_1 in simple shear flow (specifically $N_1 = 2\lambda_1\eta_{p0}\dot{\gamma}^2/f^2$, based upon Eq. (3)), where *f*-increases with rising-$\dot{\gamma}$ (see Fig. 9); and (ii) the EPTT *f*-results in complex flow, with relatively large $f = O(360)$ and large $We_{lim} = 210$ (cf. Table 4), and small N_1. In contrast, the *thixotropic MBM, NM_τ_p and NM_T results* produce relatively more intense and larger N_1 maxima zones (Fig. 12a), smaller *f* and We_{lim}. For example, at $We = 2$, MBM-N_1 is twice as large as for EPTT and NM_τ_p (cf. Table 5). The non-convoluted *f*-maxima range is from {$f = O(1)$, $We = 0.1$} to {$f = O(20)$, $We = O(10)$} (cf. Table 4). Consequently, critical elasticity levels are much smaller and lie around $We_{lim} = O(10)$. In Fig. 13a (*f-functional fields non-convoluted*), notable differences in EPTT *f*-field results are apparent relative to the non-convoluted thixotropic solutions from low *We* levels ($We = 0.5$). EPTT data show a red-intense zone with relatively large, positive values about the contraction. As *We* is increased, the EPTT red zone grows in size and magnitude notably, from $f = O(10)$ at $We = 0.1$, to $f = O(10^2)$ at $We = 100$ (Table 4); until almost filling the region about the contraction. Moreover, localised small-*f* zones are apparent at the re-entrant and downstream corner for EPTT solutions at $We = 50$ and onwards. Contrastingly, the micellar MBM, NM_τ_p and NM_T *f*-field results do not exhibit such growth in size and intensity as *We* is elevated. Indeed, these results exhibit a blue-light zone with relatively small, and even negative, values arising from the centreline. This is shifted downstream and lies within the red zone. Conspicuously and in contrast to EPTT *f*-fields, the micellar *f*-fields reveal that the blue patch at the contraction grows until it touches the wall, before encountering numerical solution breakdown.

4.3.5. Convoluted versus non-convoluted, f-maximum values at We_{lim} (Tables 4 and 5), f-fields

In this comparison, significantly larger *f*-maxima are obtained for the EPTT and convoluted versions (*exponential f*), relative to their non-convoluted thixotropic analogues (*linear f*) at their respective We_{lim}: in fact, one order of magnitude larger. Specifically, EPTT/MBM results render $f = O(390)$, whilst MBM predicts $f = O(7)$, and EPTT originate $f = O(360)$. Similarly, EPTT/NM_τ_p and NM_τ_p data result in $f = O(400)$ and $f = O(10)$, respectively. Moreover, EPTT/NM_T solutions evidence $f = O(500)$ at $We = 300$ and beyond, whilst NM_T results show $f = O(20)$ at its We_{lim}. Accordingly, the convoluted N_1-values are smaller than for the non-convoluted counterparts (Table 5), and decline as *We* is

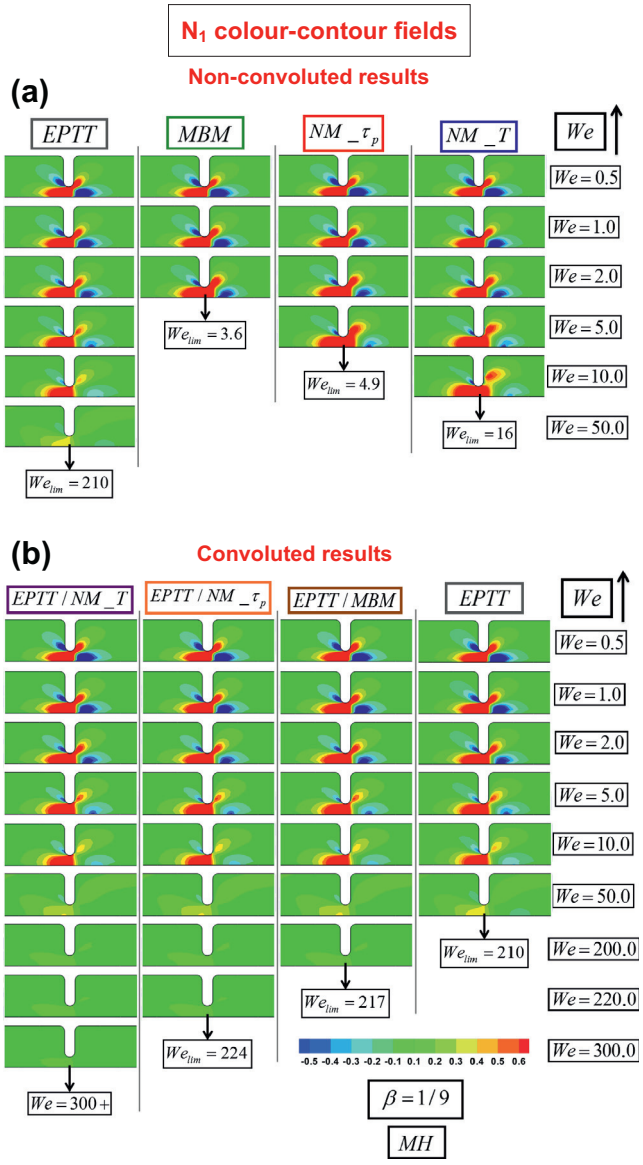

Fig. 12. N_1 fields versus *We*: (a) EPTT, MBM, NM_τ_p and NM_T models, (b) EPTT, EPTT/MBM, EPTT/NM_τ_p and EPTT/NM_T models; MH (EPTT $\varepsilon = 0.25$; Micellar $\omega = 4.0$) response, highly-polymeric ($\beta = 1/9$) fluids.

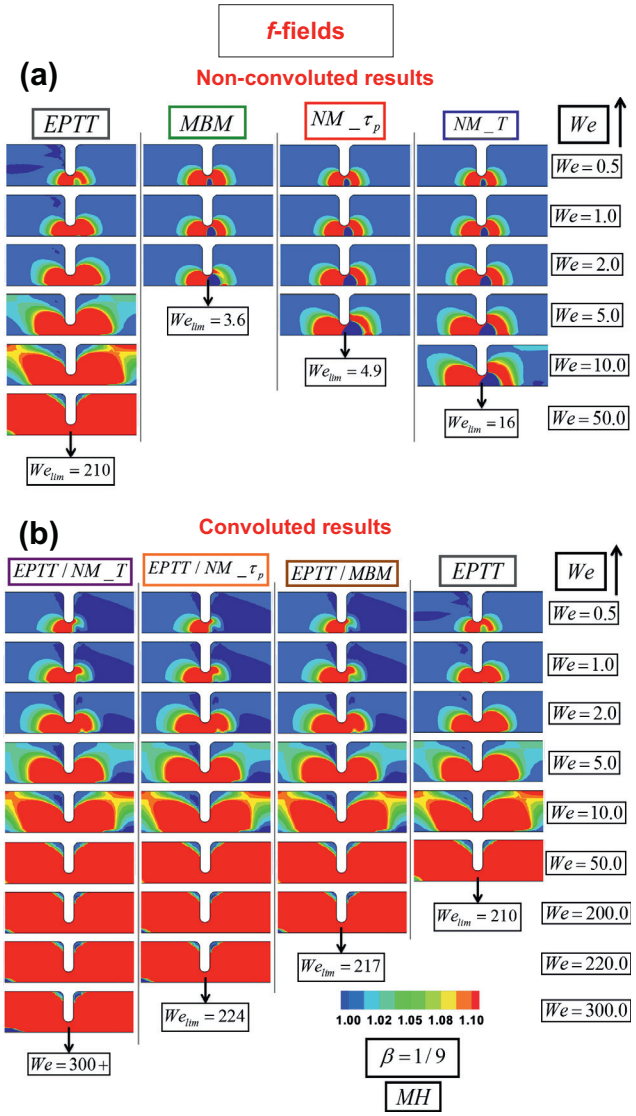

Fig. 13. *f*-Function fields versus *We*: (a) EPTT, MBM, NM_τ_p and NM_T models, (b) EPTT, EPTT/MBM, EPTT/NM_τ_p and EPTT/NM_T models; MH (EPTT $\varepsilon = 0.25$; Micellar $\omega = 4.0$) response, highly-polymeric ($\beta = 1/9$) fluids.

elevated, thus rendering larger We_{lim}. In the *f*-fields displayed in Fig. 13b, the convoluted solutions exhibit micellar features at low elasticity levels ($0.1 < We < 2.0$): a blue relatively small zone that disappears as *We* is increased, when EPTT characteristics emerge, with the growing large-*f* red zone for $We > 5.0$ onwards. Accordingly, the convoluted N_1-fields exhibit the inverse relationship with *f*-functional as *We* is elevated (Fig. 12b).

All above findings can be related to the corresponding materials functions (Figs. 1 and 2) and their impact on flow kinematics (Figs. 6a, 7, 8 and 10). Both constitutive representations, the time-independent network-based EPTT, and the time-dependent micellar models, provide shear-thinning in steady simple shear and strain-hardening/softening effects in steady simple uniaxial extension (Fig. 1). Moreover, they exhibit an inverse, quadratic relation between N_1 and *f* in viscometric simple shear flow (Fig. 12). Nevertheless, EPTT results evidence a more complex kinematics than the micellar forms (Figs. 6a, 8 and 10). Major differences in *f*-results between the EPTT and non-convoluted micellar forms become apparent. Therefore, one may argue that the manifestation of the strain-hardening and softening characteristics (on vortex size/intensity, and N_1) is influenced by the magnitude of the *f*-functional predicted in complex flow, which seems to be largely dictated by the *f*–*We* functionality. Specifically, as noted for EPTT and convoluted models, and in contrast with the strain-hardening effects observed exclusively in the thixotropic non-convoluted micellar solutions. The exponential *f*-functional of EPTT and convoluted forms (Table 1) provide impressively larger *f*-results, which generate relatively smaller N_1 values, and consistently, larger We_{lim} in complex flow. Alternatively the linear *f*-expression, as in NM_τ_p and NM_T models, yields relatively smaller *f*-predictions, with larger N_1 and smaller We_{lim} than those of EPPT. These trends become even more noticeable for the MBM predictions, a model devoid of *f*–*We* explicit functionality.

5. Conclusions

A new set of constitutive models based on the MBM model [3] for wormlike micellar solutions has been presented, involving the viscoelasticity in the structure construction/destruction mechanics. Solutions are compared between time-dependent thixotropic

MBM models and network-based time-independent EPTT models. Complex flows for a 4:1:4 rounded contraction/expansion are considered, under relatively moderate and strong strain-hardening response, and highly-polymeric and Newtonian like instances.

Analysis for the MBM model in the complex axisymmetric 4:1:4 contraction/expansion flow has provided information based on phenomenological observation (EPD attainment). Here, feedback between viscometric theory and complex flow analyses complement and improve the micellar constitutive approach, reflecting the new physics involved. In this study, this point is illustrated through the observation of the EPD underprediction at low elasticity levels, for which the MBM model provides inconsistent results, and upon which a correction is performed.

The new constitutive framework provides (a) consistent EPD predictions at low elasticity levels (contrary to the MBM model), (b) larger limiting *We* to those obtained with the MBM model, by the explicit presence of *We* in the micellar *f*-functional, and (c) rising EPD tendency at high-elasticity instances for Newtonian-like, moderate hardening fluids.

Moreover, impressively high-*We* results, of interest for industrial applications and microfluidics/nanotechnology ($We \sim 300+$), have been obtained for the models characterising micellar solutions. This was achieved through the convolution of the *f*-functional of the micellar and EPPT models. The analysis of the *f*-functional across models evidences notable trends as to the level of attainable We_{lim}. Here, models with stronger explicit mathematical functionality between *f* and λ_1 (*We*) provide larger We_{lim}. Furthermore, the effects of these large-*f* results are reflected, firstly, on the N_1 magnitude predicted. These obey the inverse, quadratic functionality between N_1 and *f*, found in simple shear flow. Secondly, as demonstrated in this study and elsewhere [47], the vortex dynamics proves to be a function of the N_2-minima, as located in the vortices generated. Moreover, the relative size of *f*-predictions influences the manifestation of strain-softening/hardening characteristics through the vortex dynamics. Thus, outstandingly definite trends are established regarding the various constitutive models proposed. Significantly, the EPTT and its convoluted solutions evidence relatively complex kinematical behaviour with *We* rise, based on the relatively large *f*-values generated. Here, increasing vortex growth to a maximum is reported for the low-to-moderate elasticity range, with further decrease to a minimum over the moderate-to-high elasticity range, and ultimate rise in the high elasticity range. In particular, this rise in vortex intensity at high *We* is related to the formation and enhancement of a second upstream vortex, which is observed with the convoluted models. In contrast, solutions with non-convoluted micellar models and relatively smaller *f*-values, provide only vortex enhancement before their earlier numerical breakdown.

Acknowledgements

Financial support (scholarship to J.E.L.-A.) from Consejo Nacional de Ciencia y Tecnología (CONACYT, México), Zienkiewcz College of Engineering scholarship and NHS-Wales Abertawe Bro Morgannwg Trust-fund, is gratefully acknowledged.

References

[1] F. Bautista, J.M. de Santos, J.E. Puig, O. Manero, Understanding thixotropic and antithixotropic behavior of viscoelastic micellar solutions and liquid crystalline dispersions. I. The model, J. Non-Newton. Fluid Mech. 80 (1999) 93–113.
[2] O. Manero, F. Baustista, J.F.A. Soltero, J.E. Puig, Dynamics of worm-like micelles: the Cox–Merz rule, J. Non-Newton. Fluid Mech. 106 (2002) 1–15.
[3] E.S. Boek, J.T. Padding, V.J. Anderson, P.M.J. Tardy, J.P. Crawshaw, J.R.A. Pearson, Constitutive equations for extensional flow of wormlike micelles: stability analysis of the Bautista–Manero model, J. Non-Newton. Fluid Mech. 126 (2005) 29–46.
[4] F. Bautista, J.F.A. Soltero, J.H. Pérez-López, J.E. Puig, O. Manero, On the shear-banding flow of elongated micellar solutions, J. Non-Newton. Fluid Mech. 94 (2000) 57–66.
[5] P.D. Olmsted, Perspectives on shear-banding in complex fluids, Rheol. Acta 47 (2008) 283–300.
[6] J. Yang, Viscoelastic wormlike micelles and their applications, Curr. Opin. Colloid Interf. Sci. 7 (2002) 276–281.
[7] E. Miller, J.P. Rothstein, Transient evolution of shear-banding wormlike micellar solutions, J. Non-Newton. Fluid Mech. 143 (2007) 22–37.
[8] R.G. Moss, J.P. Rothstein, Flow of wormlike micelle solutions past a confined circular cylinder, J. Non-Newton. Fluid Mech. 165 (2010) 1505–1515.
[9] F. Baustista, J.H. Pérez-López, J.P. García, J.E. Puig, O. Manero, Stability analysis of shear-banding flow with the BMP model, J. Non-Newton. Fluid Mech. 144 (2007) 160–169.
[10] J.P. García-Sandoval, O. Manero, F. Bautista, J.E. Puig, Inhomogeneous flows and shear-banding formation in micellar solutions: predictions of the BMP model, J. Non-Newton. Fluid Mech. 179–180 (2012) 43–54.
[11] E.E. Herrera, F. Calderas, A.E. Chávez, O. Manero, Study on the pulsating flow of a worm-like micellar solution, J. Non-Newton. Fluid Mech. 165 (2010) 174–183.
[12] Y. Caram, F. Baustista, J.E. Puig, O. Manero, On the rheological modelling of associative polymers, Rheol. Acta 46 (2006) 45–57.
[13] A.J. Mendoza-Fuentes, R. Montiel, R. Zenit, O. Manero, On the flow of associative polymers past a sphere: evaluation of the negative wake criteria, Phys. Fluids 21 (2009) 45–57.
[14] A.J. Mendoza-Fuentes, O. Manero, R. Zenit, Evaluation of drag correction factor for spheres settling in associative polymers, Rheol. Acta 49 (2010) 979–984.
[15] H.R. Tamaddon-Jahromi, M.F. Webster, J.P. Aguayo, O. Manero, Numerical investigation of transient contraction flows for wormk-like micellar systems using Bautista–Manero models, J. Non-Newton. Fluid Mech. 166 (2011) 102–117.
[16] M.R. Stukan, E.S. Boek, J.T. Padding, W.J. Briels, J.P. Crawshaw, Flow of wormlike micelles in an expansion contraction geometry, Soft Matter 4 (2008) 870–879.
[17] P.A. Vazquez, G.H. McKinley, L.P. Cook, A network scission model for wormlike micellar solutions: I. Model formulations and viscometric flow predictions, J. Non-Newton. Fluid Mech. 144 (2007) 122–139.
[18] M. Cromer, L.P. Cook, G.H. McKinley, Pressure-driven flow or wormlike micellar solutions in rectilinear microchannels, J. Non-Newton. Fluid Mech. 166 (2011) 180–193.
[19] L. Zhou, L.P. Cook, G.H. McKinley, Probing shear-banding transitions of the VCM model for entangled wormlike micellar solutions using large amplitude oscillatory shear (LAOS) deformations, J. Non-Newton. Fluid Mech. 165 (2010) 1462–1472.
[20] P.D. Olmsted, O. Radulescu, C.Y.F. Lu, Johnson–Segalman model with a diffusion term in a cylindrical Couette flow, J. Rheol. 44 (2000) 257–275.
[21] S.M. Fielding, P.D. Olmsted, Flow phase diagrams concentration-coupled shear-banding, Eur. Phys. J. E 11 (2003) 65–82.
[22] O. Radulescu, P.D. Olmsted, C.Y.F. Lu, Shear-banding in reaction-diffusion models, Rheol. Acta 38 (1999) 606–613.
[23] M.W. Libertatore, F. Nettesheim, P.A. Vazquez, M.E. Helgeson, N.J. Wagner, E.W. Kaler, L.P. Cook, L. Porcar, Y.T. Hu, Microstructure and shear rheology of entangled wormlike micelles in solution, J. Rheol. 53 (2009) 441–458.
[24] A.K. Gurnon, N.J. Wagner, Large amplitude oscillatory shear (LAOS) measurements to obtain constitutive equation model parameters: Giesekus model of banding and nonbanding wormlike micelles, J. Rheol. 56 (2012) 333–351.
[25] P. Thareja, I.H. Hoffmann, M.W. Libertatore, M.E. Helgeson, Y.T. Hu, M. Gradzielski, N.J. Wagner, Shear-induced phase separation (SIPS) with shear-banding in solutions of cationic surfactant and salt, J. Rheol. 55 (2011) 1375–1397.
[26] M.E. Helgeson, P.A. Vazquez, E.W. Kaler, N.J. Wagner, Rheology and spatially resolved structure of cetyltrimethylammonium bromide wormlike micelles through the shear-banding transition, J. Rheol. 53 (2009) 727–756.
[27] M.E. Helgeson, M.D. Reichert, Y.T. Hu, N.J. Wagner, Relating shear-banding, structure, and phase behaviour in wormlike micellar solutions, Soft Matter 5 (2009) 3858–3869.
[28] P. Fischer, H. Rehage, Non-linear flow properties of viscoelastic surfactant solutions, Rheol. Acta 36 (1997) 13–27.
[29] H. Rehage, H. Hoffmann, Viscoelastic surfactant solutions: model systems for rheological research, Mol. Phys. 74 (1991) 933–973.
[30] A. Parker, W. Fieber, Viscoelasticity of anionic wormlike micelles: effect of ionic strength and small hydrophobic molecules, Soft Matter 9 (2013) 1203–1213.
[31] C.A. Dreiss, Wormlike micelles: where do we stand? Recent developments, linear rheology and scattering techniques, Soft Matter 3 (2007) 956–970.
[32] S.R. Raghavan, E.W. Kaler, Highly viscoelastic wormlike micellar solutions formed by cationic surfactants with long unsaturated tails, Langmuir 17 (2001) 300–306.
[33] F. Bautista, V.V.A. Fernandez, E.R. Macias, J.H. Perez-Lopez, J.I. Escalante, J.E. Puig, O. Manero, Experimental evidence of the critical phenomenon and shear-banding flow in polymer-like micellar solution, J. Non-Newton. Fluid Mech. 177–178 (2012) 89–96.
[34] K. Walters, M.F. Webster, The distinctive CFD challenges of computational rheology, Int. J. Numer. Meth. Fluids 43 (2003) 577–596.

[35] M. Aboubacar, M.F. Webster, A cell-vertex finite volume/element method on triangles for abrupt contraction viscoelastic flows, J. Non-Newton. Fluid Mech. 98 (2001) 83–106.
[36] M. Aboubacar, H. Matallah, M.F. Webster, Highly elastic solutions for Oldroyd-B and Phan-Thien/Tanner fluids with a finite volume/element method: planar contraction flows, J. Non-Newton. Fluid Mech. 103 (2002) 65–103.
[37] M. Aboubacar, H. Matallah, H.R. Tamaddon-Jahromi, M.F. Webster, Numerical prediction of extensional flows in contraction geometries: hybrid finite volume/element method, J. Non-Newton. Fluid Mech. 104 (2002) 125–164.
[38] D.M. Binding, P.M. Phillips, T.N. Phillips, Contraction/expansion flows: the pressure drop and related issues, J. Non-Newton. Fluid Mech. 137 (2006) 31–38.
[39] J.P. Aguayo, H.R. Tamaddon-Jahromi, M.F. Webster, Excess pressure-drop estimation in contraction and expansion flows for constant shear-viscosity, extension strain-hardening fluids, J. Non-Newton. Fluid Mech. 153 (2008) 157–176.
[40] H.A. Barnes, J.F. Hutton, K. Walters, An Introduction to Rheology, Elsevier, Oxford, 1989.
[41] R. Tanner, Engineering Rheology, second ed., Oxford University Press, Oxford, 2000.
[42] N. Phan-Thien, R.I. Tanner, A new constitutive equation derived from network theory, J. Non-Newton. Fluid Mech. 2 (1977) 353–365.
[43] J.L. Guermond, L. Quartapelle, On stability and convergence of projection methods based on pressure Poisson equation, Int. J. Numer. Meth. Fluids 26 (1998) 1039–1053.
[44] P. Wapperom, M.F. Webster, A second-order hybrid finite-element/volume method for viscoelastic flows, J. Non-Newton. Fluid Mech. 79 (1998) 405–431.
[45] M.F. Webster, H.R. Tamaddon-Jahromi, M. Aboubacar, Transient viscoelastic flows in planar contractions, J. Non-Newton. Fluid Mech. 118 (2004) 83–101.
[46] K. Walters, H.R. Tamaddon-Jahromi, M.F. Webster, M.F. Tomé, S. McKee, The competing roles of extensional viscosity and normal stress difference in complex flows of elastic liquids, Korea-Aust. Rheol. J. 21 (2009) 225–233.
[47] H.R. Tamaddon-Jahromi, M.F. Webster, Transient behaviour of branched polymer melts through planar abrupt and rounded contractions using pom-pom models, Mech. Time-Depend. Mater 15 (2011) 181–211.